

Antimony(III)-Doped PbWO₄ Crystals with Enhanced Photoluminescence via a Shape-Controlled Sonochemical Route

Jun Geng,^{†,‡} Dujuan Lu,[†] Jun-Jie Zhu,^{*,†} and Hong-Yuan Chen[†]

Key Laboratory of Analytical Chemistry for Life Science, School of Chemistry and Chemical Engineering, Nanjing University, Nanjing 210093, P. R. China, and Department of Chemistry, Jiangsu Institute of Education, Nanjing 210013, P. R. China

Received: December 29, 2005; In Final Form: May 17, 2006

Sb(III)-doped lead tungstate single crystals with controlled shapes and enhanced green emission have been synthesized via a facile, Pluronic P123 (EO₂₀PO₇₀EO₂₀)-assisted, sonochemical method. The surfactant Pluronic P123 was found to play a crucial role in the morphology control of the final products. The growth process was investigated by carefully following time-dependent experiments, and the oriented attachment process accompanying Ostwald ripening was proposed for the possible formation mechanism. The optical properties, such as the Raman spectra and PL spectra, of doped PbWO₄ were studied. Room-temperature photoluminescence of doped PbWO₄ samples with different morphologies at desired Sb doping concentrations showed greatly enhanced luminescence intensity compared to the undoped PbWO₄.

Introduction

The properties of nanomaterials are determined significantly by their structures, i.e., by their dimensions, crystallinity, and geometry.¹ Novel synthetic approaches could lead to the discovery of novel nanostructures with new properties.

In recent years, ultrasound has become an important tool in chemistry for its applications in the synthesis and modification of both organic and inorganic materials.^{2–4} When liquids are irradiated with high-intensity ultrasound, acoustic cavitations (the formation, growth, and implosive collapse of the bubbles) provide the primary mechanism for sonochemical effects, during which very high temperatures (> 5000 K), pressures (> 20 MPa), and cooling rates (> 10¹⁰ K/s) can be achieved upon the collapse of the bubbles.⁵ Such remarkable environments provide a unique platform for the growth of novel nanostructures.

Lead tungstate (PbWO₄) has been attracting increasing attention because of its technological importance as an inorganic scintillating crystal. Compared to other well-known scintillators, PbWO₄ is most attractive for high-energy physics applications because of its high density (8.3 g/cm³), short decay time, high-irradiation damage resistance, interesting excitonic luminescence, thermoluminescence, and stimulated Raman scattering behavior.^{6,7} Since PbWO₄ has the structure sensitivity and its luminescence is remarkably affected by the structure defects in the crystals, improving its scintillating properties through changing and controlling its structure defects, such as appropriate doping and annealing in proper atmosphere, has become one of the principal methods in the research on PbWO₄.^{8,9} Doping with ions can adjust the defects in pure PbWO₄ and decrease or even eliminate some harmful defects although these ions themselves are impurity defects. Antimony has been tried as a beneficial doping impurity recently. Sb-doped PbWO₄

(PbWO₄:Sb) does show greater transmittance and radiation hardness, as well as better luminescence intensity and light yield.^{10,11}

Sb-doped PbWO₄ single crystals have usually been grown from the melt using the Czochralski^{12,13} and Bridgeman^{14–16} methods. To the best of our knowledge, the wet-chemical synthesis of doped PbWO₄ has not been reported, especially with controlled shapes. Herein, we have prepared single-crystalline PbWO₄:Sb via a facile sonochemical route in the aqueous solution. By using the triblock copolymer (PEO–PPO–PEO) as crystal growth modifier, Sb-doped PbWO₄ crystals with novel structures and different morphologies can be efficiently achieved. The effect of Sb doping on the optical properties of PbWO₄ was examined. Compared with the luminescence of undoped PbWO₄ that was grown under the same circumstance, the PL intensity of Sb-doped PbWO₄ was greatly enhanced.

Experimental Section

Materials. All the reagents used were of analytical purity and used without further purification. The Pluronic amphiphilic triblock copolymer P123 (EO₂₀PO₇₀EO₂₀, M_{av} = 5800) was obtained from Aldrich. Pb(CH₃COO)₂·3H₂O, Na₂WO₄·2H₂O, SbCl₃, and absolute ethanol were purchased from Shanghai Second Chemical Reagent Factory (Shanghai, China).

Synthesis. Pb(CH₃COO)₂·3H₂O (0.38 g, 1 mmol) was added to an (EO)₂₀–(PO)₇₀–(EO)₂₀ solution (10 g·L⁻¹, 100 mL) under vigorous stirring to give a clear and homogeneous solution. A 1 mL volume of SbCl₃ solution (1 mM, 0.1 mol %) was introduced to the above solution. Another 1 mL aqueous solution of Na₂WO₄ (1 M) was added into the above mixture under vigorous stirring. Then the mixture was exposed to high-intensity ultrasound irradiation under ambient air. Ultrasound irradiation was accomplished with a high-intensity ultrasonic probe (Xinzhi Co., Ningbo, China, JY92-2D, 0.6 cm diameter; Ti-horn, 20 kHz, 60 W/cm²) immersed directly in the reaction solution, and the total reaction time lasted for 30 min. A white precipitate was centrifuged, washed with distilled water and absolute ethanol in sequence, and finally dried in air. In the experiments,

* To whom correspondence should be addressed. E-mail: jjzhu@netra.nju.edu.cn; zhujunjie@nju.org.cn. Tel and Fax: +86-25-83594976.

[†] Nanjing University.

[‡] Jiangsu Institute of Education.

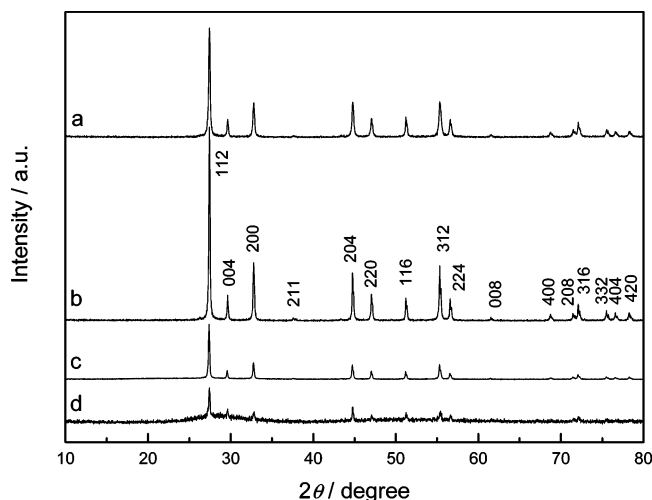


Figure 1. XRD patterns of (a) pure PbWO_4 , and Sb-doped PbWO_4 samples prepared under copolymer concentrations of (b) $10 \text{ g}\cdot\text{L}^{-1}$, (c) $20 \text{ g}\cdot\text{L}^{-1}$, and (d) $40 \text{ g}\cdot\text{L}^{-1}$. (The initial concentrations of Pb^{2+} and WO_4^{2-} were both 10 mM , and the doping concentration of Sb was $0.1 \text{ mol } \%$.)

the concentration of P123 was varied from 10 to $40 \text{ g}\cdot\text{L}^{-1}$, and the doping concentration of SbCl_3 was varied from 0.05 to $1 \text{ mol } \%$.

Characterization. The X-ray powder diffraction (XRD) analysis was performed by a Philips X'pert X-ray diffractometer at a scanning rate of $4^\circ/\text{min}$ in the 2θ range from 10 to 80° , with graphite-monochromatized $\text{Cu K}\alpha$ radiation ($\lambda = 0.15418 \text{ nm}$). Field-emission scanning electron micrographs (FE-SEM) were taken on a LEO-1530VP field-emission scanning electron microscope. Transmission electron micrographs (TEM) and selected area electron diffraction (SAED) patterns were recorded on a JEOLJEM 200CX transmission electron microscope, using an accelerating voltage of 200 kV . High-resolution transmission electron micrographs (HRTEM) were obtained by employing a JEOL-2010 high-resolution transmission electron microscope with a 200 kV accelerating voltage. Raman spectra were recorded on a JY HR-800 spectrometer provided by J. Y. Co. at room temperature with an excitation wavelength of 488 nm . Photoluminescence spectra were measured on a SLM48000DSCF/AB2 fluorescence spectrometer made by American SLM Inc. at room temperature. The powder of final product was impact into a silica groove (with dimension of $10 \times 3 \times 3 \text{ mm}^3$) for measurement.

Results and Discussion

Characterizations of Final Products. The XRD profiles of pure and doped PbWO_4 samples ($0.1 \text{ mol } \%$ Sb) are shown in Figure 1. All the peaks are well indexed by tetragonal $I4_1/a$ in the JCPDS cards (JCPDS Card No. 08-0476), which reveals that the doping of Sb at designed concentration does not change the crystal structure or induce a new phase. The crystals are of homogeneous stolzite structure with good quality, and the Sb ions would go into PbWO_4 crystal lattice well. On comparing the curves of the products synthesized under different copolymer concentrations, we found that the relative intensity of the peaks varied significantly, which indicates different crystallinity. The sample prepared in the $10 \text{ g}\cdot\text{L}^{-1}$ P123 system shows better crystallization than the other two samples. The cell parameters of crystals with different doping concentrations were also investigated, and the results are listed in Table 1. It is found that the values of a and c both decreased with the introduction of impurities, which is consistent with the fact that the radii of

TABLE 1: Cell Parameters of Pure and Doped PbWO_4 Crystals Prepared in a $10 \text{ g}\cdot\text{L}^{-1}$ P123 System

sample	doping concn (mol %)	a (Å)	c (Å)
pure PbWO_4	0	5.469 04	12.049 43
$\text{PbWO}_4\text{:Sb}$	0.05	5.463 17	12.044 42
$\text{PbWO}_4\text{:Sb}$	0.1	5.461 19	12.044 10
$\text{PbWO}_4\text{:Sb}$	0.2	5.460 38	12.039 65

Sb^{3+} ($R = 0.76 \text{ Å}$) is smaller than that of Pb^{2+} ($R = 1.20 \text{ Å}$). As reported for the La-doped PbWO_4 , the cell parameters diminish with increasing La^{3+} content;¹⁷ a similar trend was also observed in our experiments.

The morphologies of the synthesized products were examined by FE-SEM and TEM. Typical FE-SEM images of the product prepared in the system of $10 \text{ g}\cdot\text{L}^{-1}$ P123 at room temperature are shown in Figure 2. All the samples are special starlike dendritic structures, and the individual dendrite with a three-dimensional structure displays complex features (Figure 2a). There are one main trunk and four crossed branches extending from the center of the main trunk, which construct the framework with a scalariform manner. From the top view of the SEM image (Figure 2b), we can see that the crossed branches construct the framework in a perfect perpendicular manner and the 4-fold symmetry of the structure can be identified. The whole length of the main trunk is about $1.5 \mu\text{m}$, and the maximum length of the four branches is about 250 nm measured from the center of main trunk. Careful observation shows that the dendrite is composed of directly arrayed nanopolyhedrons that are attached to each other in an interesting parallel and scalariform way rather than in a simple manner.

Figure 2c,d shows the FE-SEM images of the product obtained in another system containing $20 \text{ g}\cdot\text{L}^{-1}$ P123. All the samples are homogeneous spindlelike nanorods with diameter of 220 nm at the center and length of about $1.5 \mu\text{m}$ (Figure 2c). High-magnification SEM images (Figure 2d) reveal that the spindles are also constructed from assembled nanopolyhedrons and a hierarchical structure similar to the above dendritic structure can be detected.

The morphology of the products varied greatly when the concentration of P123 changed to $40 \text{ g}\cdot\text{L}^{-1}$ while the other conditions were kept the same. A typical FE-SEM image (Figure 2e) shows that the product consists of a large quantity of nanospheres with uniform size distribution of diameter about 300 nm . A high-magnification SEM image (Figure 2f) shows that the surface of the nanosphere is quite smooth.

HRTEM images recorded on an individual dendrite and spindle provide further insight into their structures. HRTEM images of the dendrite show that the product is well crystallized and exhibits a clear crystal lattice. The interplanar spacings of 0.32 and 0.30 nm could be finely detected on the tip of the main trunk (Figure 3b). The (112) and (004) crystal faces could therefore be confirmed, which shows that the main trunk grew preferentially along the c axis. The clear lattice spacing of (112) faces could also be found on the fringe of the central region on one branch (Figure 3c), which shows that the sample is structurally uniform with an oriented crystallographic direction. The same crystal lattice observed in the different regions of a dendrite suggests that the attached building blocks share the same crystal direction.

The HRTEM image recorded on the tip of a spindlelike nanorod (Figure 3e) indicates well-defined lattice fringes with interplanar spacing of 0.32 nm for the (112) faces of tetragonal PbWO_4 , indicating the high crystallinity of the product.

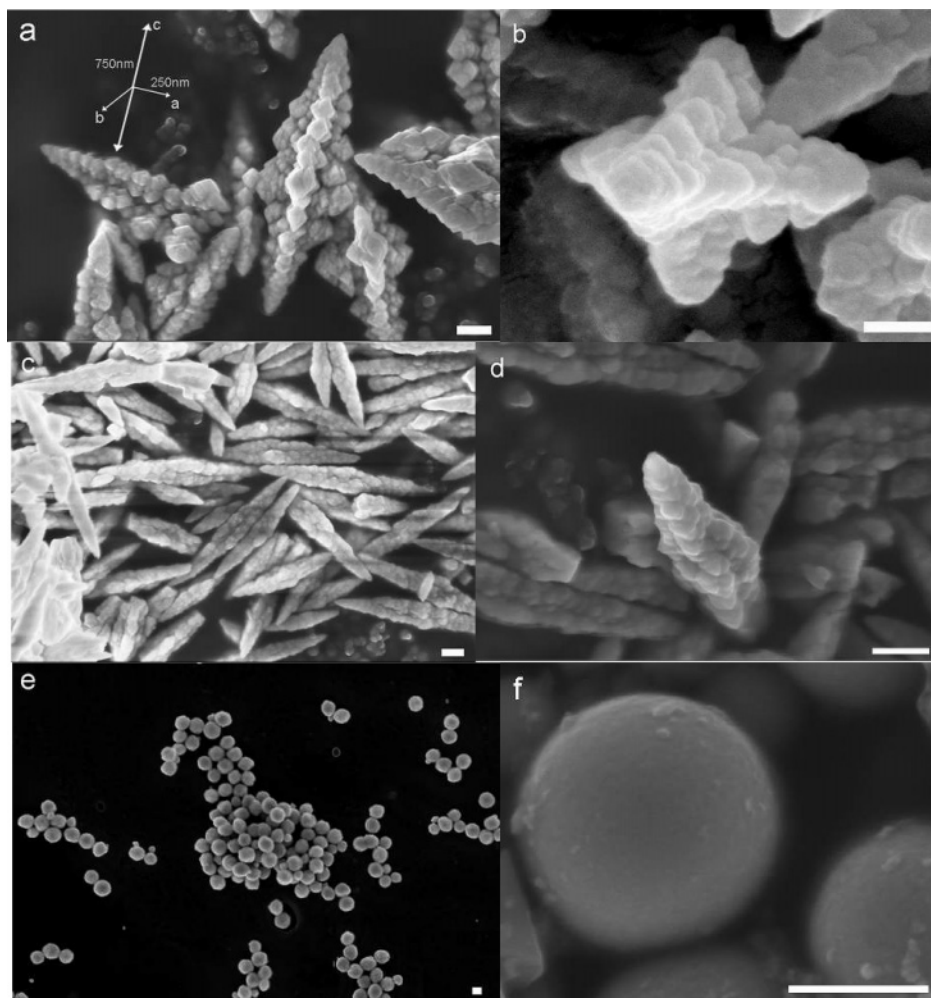


Figure 2. SEM images of a (a) side view and (b) top view of the dendritic sample synthesized in $10 \text{ g}\cdot\text{L}^{-1}$ P123, (c) low-magnification and (d) top view of the homogeneous spindlelike sample prepared in $20 \text{ g}\cdot\text{L}^{-1}$ P123, and (e) low-magnification and (f) high-magnification of a spherical sample prepared in $40 \text{ g}\cdot\text{L}^{-1}$ P123. The scale bar represents 200 nm.

Combined with SAED pattern, the preferential growth orientation along the c axis could be confirmed.

Effect of Triblock Copolymer Concentration. The physical properties of crystalline materials depend on crystal habit, grain size, and impurities or on the presence of structural modifications. In the crystallization processes from solution, the above parameters can be controlled by additives that influence nucleation, crystal growth, and aggregation of the crystals and are thus important for technical applications.¹⁸

Poly(ethylene oxide)–poly(propylene oxide)–poly(ethylene oxide) (PEO–PPO–PEO) block copolymers are well-known as dispersion stabilizers,^{19,20} pharmaceutical ingredients,^{21,22} biomedical materials,^{23,24} and templates for the synthesis of mesoporous materials and nanoparticles.^{25–28} Variation of the PEO–PPO–PEO block copolymer molecular characteristics, concentration, and temperature allows for unique modulation of block copolymer self-assembly in the presence of selective solvents such as water.^{29,30} P123 possesses a long poly(propylene oxide) segment and two medium length poly(ethylene oxide) blocks and has a relatively high molecular weight ($M_{\text{av}} = 5800$). Such a combination favors the formation of micelles, which have dehydrated poly(propylene oxide) blocks in their cores and coronas of hydrated poly(ethylene oxide) segments at the micellar surface, at low surfactant concentrations (low critical micellization concentration, cmc) and at low temperatures (low critical micellization temperature, cmt).³¹

Although the exact roles of P123 on the present crystal growth are still to be not completely understood, the triblock copolymer might play a role for at least two aspects: preventing the aggregation of PbWO_4 nanoparticles in the initial nucleation stage through coordination with Pb(II) ions³² and kinetically controlling the growth rates of various crystallographic facets of PbWO_4 through selectively adsorbing on these facets. In P123-rich solution, Pb(II) ions were surrounded and protected by P123 molecules by forming $\text{Pb}-(\text{PEO}-\text{PPO}-\text{PEO})$ units. When the system was irradiated with ultrasound, the WO_4^{2-} ions might attack the $\text{Pb}-(\text{PEO}-\text{PPO}-\text{PEO})$ units and replace the P123 molecules to form PbWO_4 nanoparticles. In the later growth stage, P123 molecules could selectively adsorb onto some surfaces of PbWO_4 crystals through O–Pb bonding, which could significantly decrease the growth rates of these surfaces and lead to highly anisotropic growth.³³

With the increase of P123 concentration, the morphology of the final products changed from 3D starlike dendrites to 1D spindlelike nanorods and then to uniform nanospheres. That is, the tendency to grow along a certain direction had been weakened to some extent. As we have analyzed with FE-SEM and HRTEM techniques, the product prepared in the presence of $10 \text{ g}\cdot\text{L}^{-1}$ P123 grew along the c axis preferentially and stretched from the major trunk in two directions, leading to a hierarchical structure. Careful observation to the FE-SEM image shows that the spindlelike structure prepared in $20 \text{ g}\cdot\text{L}^{-1}$ P123

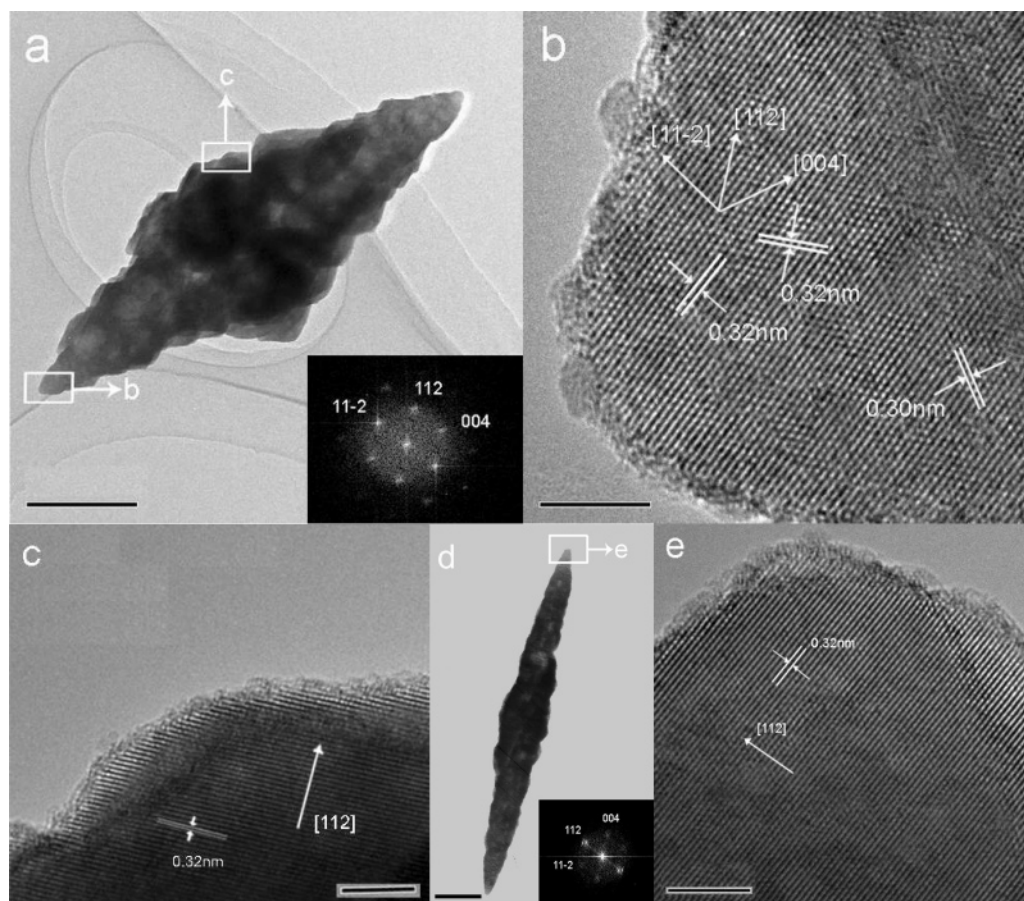


Figure 3. (a) TEM image and SAED pattern of the dendritic sample, HRTEM images recorded (b) on the tip of a dendrite and (c) on the fringe of central region, (d) TEM image and SAED pattern of a spindlelike sample, and (e) HRTEM image recorded on the tip of a spindle. (The HRTEM images were taken from the range covered in the white rectangular frames.) The scale bars in (a) and (d) represent 200 nm, and those in (b), (c), and (e) represent 5 nm.

is a bit similar to the above dendrite structure. The lengths of the major trunk of the two structures are both $1.5\ \mu\text{m}$, and the major trunks both grew along the c axis. The difference lies in the stretching extent of the crystals in the a and b directions. The dendrites exhibit more preferential crystal growth in these two directions than the spindlelike structure does. Therefore, with the increase of copolymer concentration, the crystal growth in the a and b directions has been weakened. When the P123 concentration increased to $40\ \text{g}\cdot\text{L}^{-1}$, the spheres appeared as a final structure, which displayed the isotropy in crystal growth and indicated the presence of nonspecific polymer–crystal interactions.^{34,35}

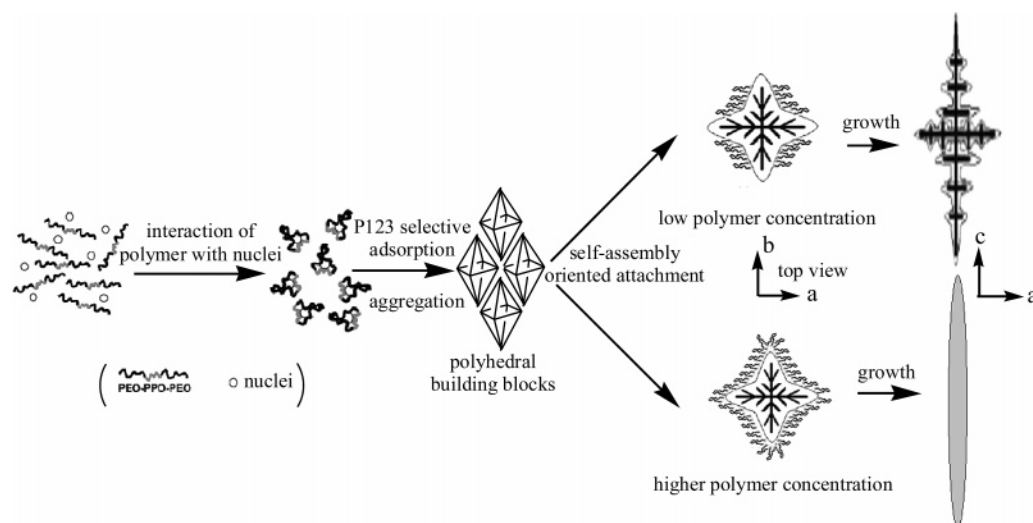
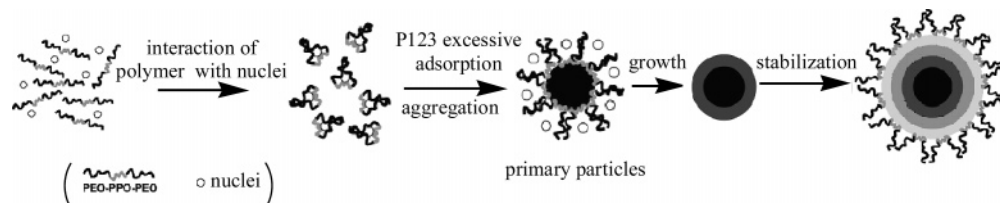
Obviously, the copolymer concentration played a key role in the shape-controlled synthesis. Reasons for this result may lie in different adsorption efficiency of surfactant molecules on specific surfaces, different growth rate, and the unusual crystal habits of PbWO_4 . The contribution of copolymer concentration to size and morphology is most likely due to the polymer adsorption on the surface of clusters. Block copolymer micelles may attach on the surface of particles above the cmc preventing the reaction monomers from approaching those planes.³⁶ The exposed faces of PbWO_4 crystals do show different polarity patterns and averaged interface energies and adsorb the copolymer with different efficiencies. The polymer-modified crystal would grow into the direction where the crystallization hindrance is weakest.³⁷

We assume that the crystal growth rate might be faster in the a , b , and c directions than in other directions; therefore, the three directions became the preferential grow orientations under

relatively low copolymer concentration. With the increasing copolymer concentration, more P123 molecules would also predominantly adsorb on the crystal faces in the a and b directions and prevent these faces from growing further. So the spindlelike product obtained in the system of $20\ \text{g}\cdot\text{L}^{-1}$ P123 appeared slimmer than the dendrites in the $10\ \text{g}\cdot\text{L}^{-1}$ P123 system. With an even higher copolymer concentration ($40\ \text{g}\cdot\text{L}^{-1}$), a spherical structure could be obtained, which suggests that the copolymer concentration is high enough to adsorb on the crystal faces in all directions to form isotropic growth. The effect of P123 on the crystal growth can be found in the illustrations of Schemes 1 and 2.

Possible Growth Mechanism and Effect of Ultrasonic Irradiation. To further investigate the details of the formation of final samples, the growth processes of the final products were carefully followed by time-dependent experiments. TEM images obtained after different reaction times show an obvious growth process from small primary nanoparticles to the final products (Figures 4, 6, and 7).

In the case of the dendritic sample, white precipitates appeared right after the reactant solution was exposed to ultrasound treatment, which indicates the nucleation took place rapidly. Small primary particles with average diameter of about 10 nm were observed in the early reaction time of 10 min (Figure 4a). These nanoparticles further aggregated in some specific orientations to form pagoda-like polyhedral structures (Figure 4b,c) that are somewhat similar to the intermediate observed by Yu et al.³⁸

SCHEME 1: Illustration of the Formation Mechanism of the Dendritic and Spindlelike Samples**SCHEME 2: Illustration of the Formation Mechanism of the Spherical Sample**

To investigate the detailed structure of the polyhedral aggregation, SEM and HRTEM techniques were also used. SEM images clearly reveal that the intermediate structures are composed of self-assembled nanopolyhedrons that attached to each other in an interesting parallel way (Figure 5a,b). The elongated octahedrons as building blocks could be detected, and an end-to-end self-assembly of these octahedrons could be speculated (Figure 5c). HRTEM images from these polyhedrons (Figure 5e) show the fringe spacing along the different directions

as 0.32 and 0.30 nm for the (112) and (004) planes, respectively, which underlines the fact that the attached building blocks share the same crystal direction with the final dendrites.

It can be speculated that the final dendritic structure evolved from such aggregates, which grew preferentially along the *c* axis after reaction for some time. A spontaneous “landing” of the small nanopolyhedrons on the backbone of the dendrites and then the undergoing crystallization could be detected, which may be related with one proposed mechanism so-called “ori-

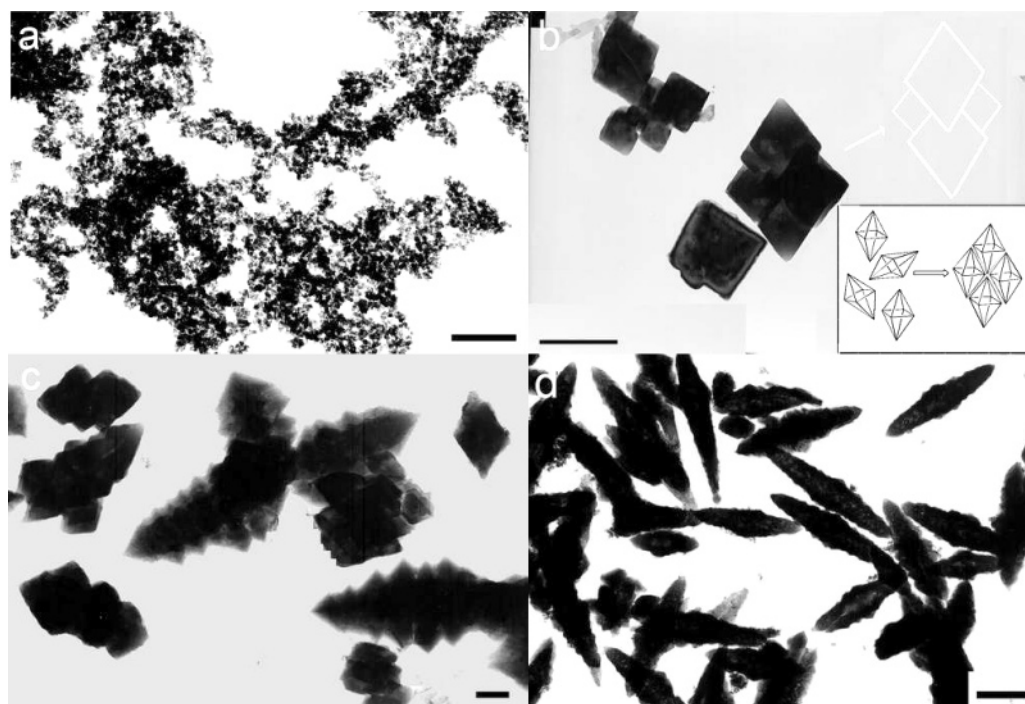


Figure 4. TEM images of dendritic sample obtained after sonication for (a) 5, (b) 15, (c) 20, and (d) 25 min. The attachment of polyhedrons in a special way could be detected. The scale bar represents 200 nm.

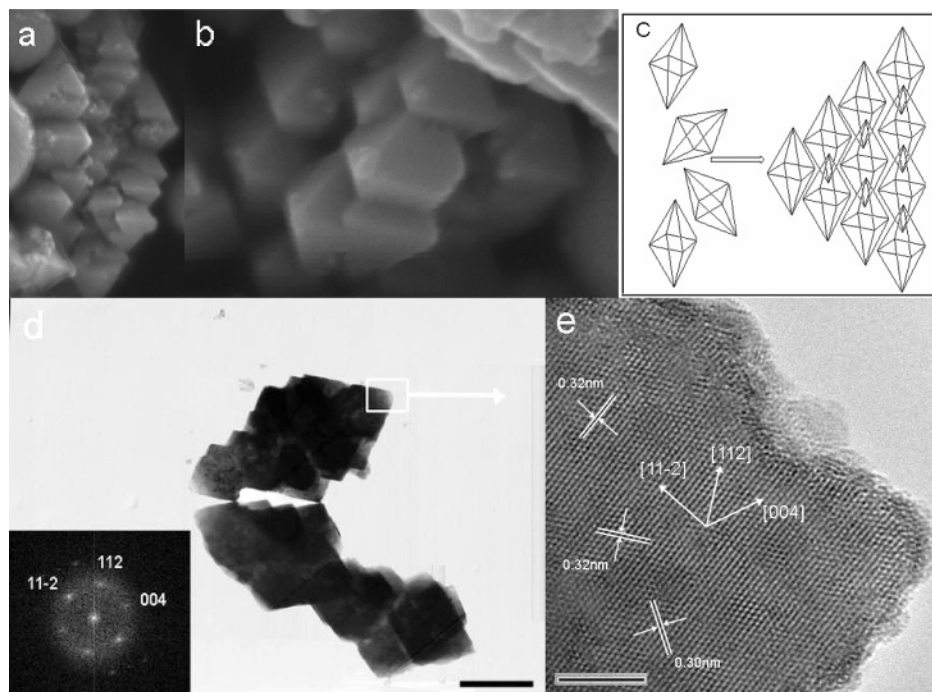


Figure 5. (a, b) SEM images of the intermediate polyhedral structures obtained after sonication for 20 min, (c) schematic illustration of the self-assembly of these nanopolyhedrons, (d) SAED pattern (scale bar represents 200 nm), and (e) HRTEM image recorded on the tip of an individual polyhedron. (The scale bar represents 5 nm.)

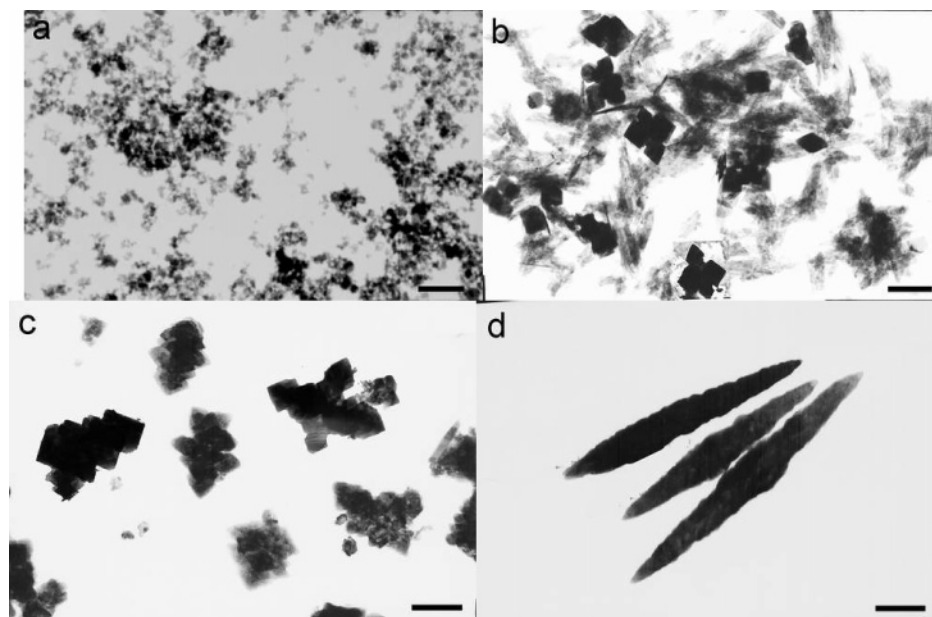


Figure 6. TEM images of a spindlelike sample obtained after sonication for (a) 5, (b) 10, (c) 15, and (d) 25 min. The scale bar represents 300 nm.

entated attachment” by Penn and Banfield.³⁹ In this mechanism, the bigger crystals are grown from small primary building blocks through an orientated attachment process, in which the adjacent building blocks are self-assembled by sharing a common crystallographic orientation and docking of these particles at a planar interface.³⁹ Primary particles may aggregate in an oriented fashion to produce a larger single crystal, or they may aggregate randomly and reorient, recrystallize, or undergo phase transformations to produce larger single crystals. This kind of growth mode could lead to the formation of faceted particles or anisotropic growth if there is sufficient difference in the surface energies of different crystallographic faces.⁴⁰ In the so-formed aggregates, the crystalline lattice planes may be almost perfectly

aligned or dislocations at the contact areas between the adjacent particles lead to defects in the finally formed bulk crystals.³⁹

However, the Ostwald ripening⁴¹ process also contributes to the formation of such structures by “shearing” the polyhedrons with sharpened edges into the blunt ones with rounded edges in their ripened final stage.

It is interesting that primary nanoparticles and similar pagoda-like nanopolyhedrons were also detected in the early growth process of the spindlelike structure (Figure 6). So we suggest that the nucleation and the initial crystal growth of these two structures might have similarities and the copolymer might play a more important and specific role in the later crystal growth stage than in the early stage under present circumstances.

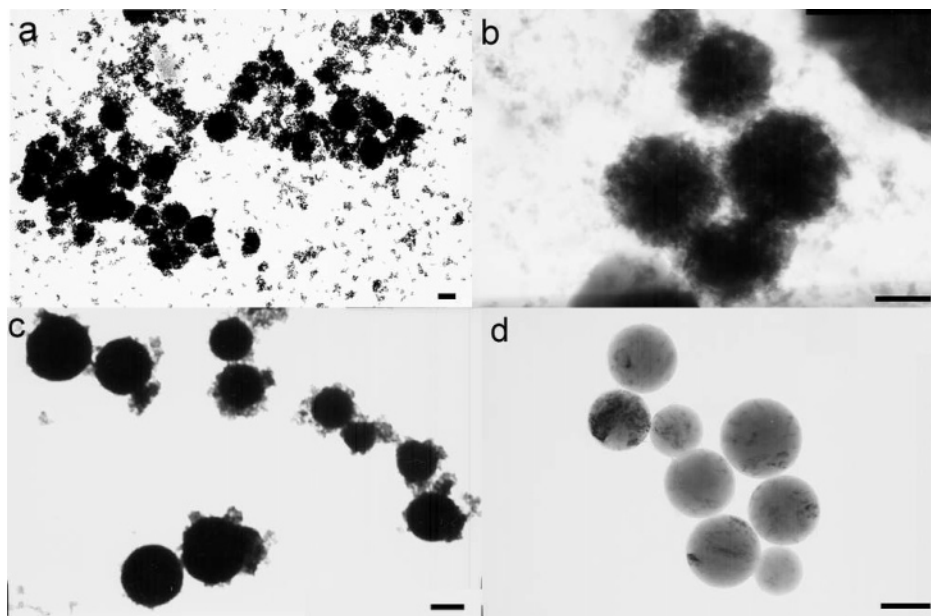


Figure 7. TEM images of a spherical sample obtained after sonication for (a) 10, (b) 15, (c) 20, and (d) 25 min. The scale bar represents 200 nm.

Different adsorption efficiencies of P123 on specific facets may contribute to the different morphologies under different concentrations, as mentioned above. Illustrations of the formation mechanism of dendrites and spindles are shown in Scheme 1.

The observation on the growth process of a spherical sample (Figure 7) reveals that the first appeared primary nanoparticles experienced further self-organization, leading to the formation of spherelike aggregates (Figure 7a). These aggregates then underwent further growth and crystallization, changing from spheres with a coarse surface to a final product with smooth surface (Figure 7b–d). The formation mechanism of spherical product is shown in Scheme 2.

In the preparation of the shape-controlled PbWO₄:Sb crystals, high-intensity ultrasound irradiation also played an important role. The transient high-temperature and high-pressure field produced during ultrasound irradiation provides a favorable environment for the anisotropic growth of nanocrystals. Cavitations and shock waves created by ultrasound can accelerate solid particles to high velocities leading to interparticle collisions and inducing effective fusion at the point of collision.⁴² We consider that ultrasound caused the fusion of adjacent particles and the attachment of primary particles on the intermediate polyhedral or spherical aggregates to form final structures. The energy generated during collision can induce the crystallization of the amorphous particles, responsible for the further crystallization process. High-intensity ultrasound irradiation is found to be necessary for the shape-controlled synthesis because comparative experiments under vigorous electric stirring instead of ultrasound treatment could not obtain the same structures.

Raman Spectra. The optical properties of these products were also studied. The Raman spectrum of the stolzite dendritic structure at an Sb doping concentration of 0.1 mol % (Figure 8) shows six bands in the range 100–1000 cm⁻¹. The peaks located at 903.3, 765.5, 749.0, 353.6, and 326.2 cm⁻¹ correspond to the vibration modes $\nu_1(A_g)$, $\nu_3(B_g)$, $\nu_3(E_g)$, $\nu_2(B_g)$, and $\nu_2(A_g)$, respectively, which are consistent with those of undoped PbWO₄ crystals reported previously.^{38,43} The peak at 175.1 cm⁻¹ was not assigned by Ross,⁴⁴ but Griffith observed a similar peak in natural and synthetic stolzite samples⁴⁵ and this peak could be assigned as the translational mode of the WO₄ group analogous to that for CdMoO₄.⁴³ The Raman spectra of crystals

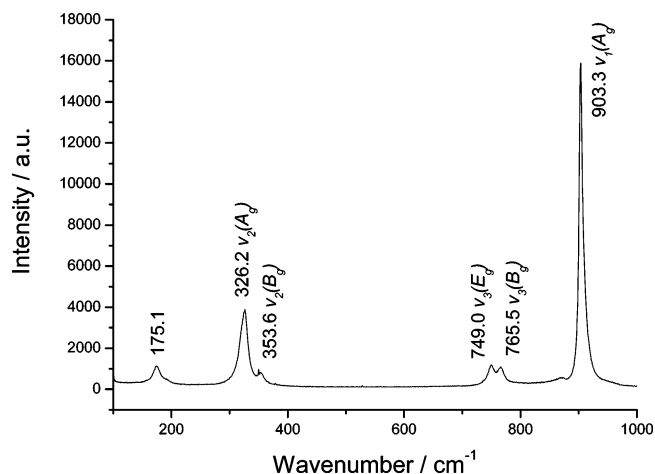


Figure 8. Raman spectrum of dendritic PbWO₄ at Sb doping concentration of 0.1 mol %.

with spindlelike and spherical shapes (Figure S1 in the Supporting Information) are similar to that of the dendritic structure.

The Raman spectra of products at different doping concentrations were also investigated (Figure S2 in the Supporting Information). With doping concentrations that ranged from 0.05 to 0.2 mol %, the Raman spectra remained the same as above. However, when the Sb doping concentration increased to 1 mol %, the Raman spectrum showed miscellaneous peaks in addition to peaks belonging to pure PbWO₄. This phenomenon indicated that heavy doping would change the original vibration of the PbWO₄ molecules.

Photoluminescence Properties. Figure 9 shows the room-temperature photoluminescence spectra of pure and 0.1 mol % Sb-doped PbWO₄ with different morphologies using the same excitation line at 300 nm. The emission of the undoped PbWO₄ is very weak and shows the intrinsic blue emission band peaks at 430 and 460 nm. The emission intensity of PbWO₄:Sb is increased enormously as compared with that of undoped PbWO₄. The spectra show that all of the three doped samples exhibited typical green emission peaks around 500 nm, similar to the result reported by Shi et al.¹⁴ The integral intensity of PbWO₄:Sb emission in the range 380–700 nm is 3 times higher than that of the undoped PbWO₄, which indicates an unusual

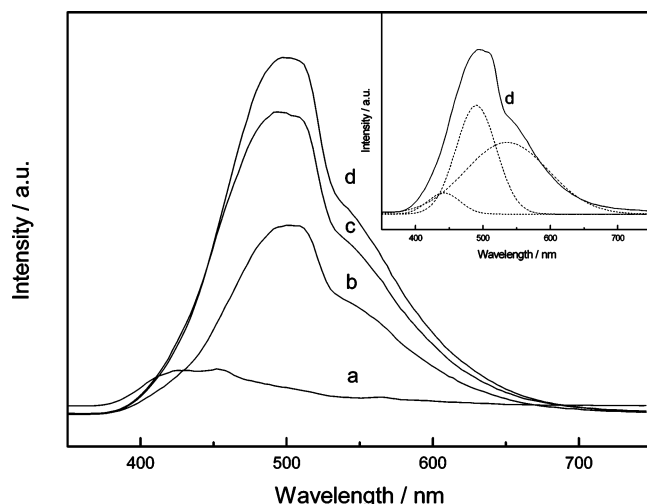


Figure 9. Room-temperature PL spectra of (a) pure PbWO_4 and Sb-doped (b) spherical, (c) spindlelike, and (d) dendritic PbWO_4 samples (0.1 mol % Sb). The inset displays the components fit curve (dashed lines) of the dendritic $\text{PbWO}_4\text{:Sb}$ sample.

improvement on the light yield by Sb doping. To simplify the comparison and discussion, we used three subbands to fit the emission curve of dendrite sample with a Gaussian distribution. The three subbands of dendritic $\text{PbWO}_4\text{:Sb}$ (see the dashed lines of the inset in Figure 9) peak at 442, 490, and 536 nm, respectively. The green subband of 490 nm offered up 50% of the total light yield. Comparison of the luminescence of the pure PbWO_4 with that of doped PbWO_4 efficiently revealed the effect of Sb doping on PbWO_4 luminescence—increasing the light yield through enhancing the green emission.¹⁴ However, as reported previously, the green component of PbWO_4 crystals is slower than the blue one in the decay characteristics.⁴⁶ Sb-doping can enhance the intensity of luminescence but may give some contributions to the “slow” decay components¹⁶ which may be negative to the scintillating properties of PWO. Further detailed investigation is needed.

Very weak size-dependent phenomenon of PL properties observed among these three products with different morphologies indicate that the sizes of the structures are so big that they are beyond the border of the quantum confinement regime. Meanwhile, the relative intensities of the PL peaks seem closely related to the morphology and crystallinity. In the three samples, the spherical product with relatively weak crystallinity shows a weaker luminescence, whereas the dendritic sample with the best crystallinity displays the strongest luminescence under the same measurement conditions. The enhancement of PL intensity may be due to the improved crystallinity, which has similarly been observed by other researchers.^{47–49} We also assume that dendritic and spindlelike crystals would possess more defects due to the faster 1-D crystal growth. These results could indicate that luminescence properties of PbWO_4 are very sensitive to its structure and strongly dependent on the crystallinity and structural defects.

We also investigated the PL properties of PbWO_4 crystals with different Sb doping concentrations. Figure 10 shows the PL spectra of the PbWO_4 crystal at Sb doping concentration varying from 0.05% to 1% in the system of 10 g·L⁻¹ P123. It is found that product with Sb doping concentration of 0.1% shows the highest PL intensity, which suggests an optimal doping concentration under current system. The heavily doped product appeared to have an extremely low PL intensity in the present case, which might be related to the changes in the

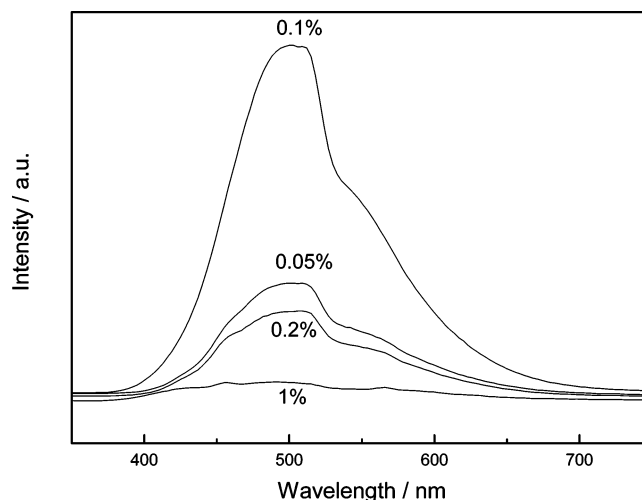


Figure 10. Emission spectra of Sb-doped PbWO_4 with different doping concentrations varying from 0.05 to 1%.

microstructure caused by heavy doping, as can be proved in its Raman spectrum mentioned above.

Conclusion

Doped lead tungstate has an important role as a functional material, and thus the rational design of its complex structures could be of significance in scintillator applications. The present experiments demonstrate, for the first time, a systematic sonochemical synthesis of Sb-doped PbWO_4 crystals with novel structures and controlled morphologies by using triblock copolymer P123 as a crystal growth modifier. The concentration of the copolymer was examined, and experimental results show its significant effects on the morphology of the final products, demonstrating that the ability of the copolymer to interact with the inorganic crystals could be fine-tuned. The formation and evolution of doped PbWO_4 structures were investigated, and the oriented attachment process accompanying Ostwald ripening was proposed as a possible growth mechanism. Successful doping is evident from the luminescence spectra of the materials. Room-temperature photoluminescence of products with different shapes and different doping concentrations show typical and enormously enhanced green emission as compared with that of undoped PbWO_4 . These as-prepared PbWO_4 nanostructures may be very attractive candidate as building blocks to build or upgrade the small functional setups for the high-energy physics region, and the ultrasound-assisted method may be a universal route to synthesize the doped PbWO_4 crystals and other luminescent crystals.

Acknowledgment. We thank Professor Guobing Ma for his skillful measurements on SEM and Professor Yinong Lv for his skillful measurements on HRTEM. This work is supported by the National Natural Science Foundation of China (Grant Nos. 20325516, 90206037, 20521503).

Supporting Information Available: Raman spectra of spindlelike and spherical PbWO_4 crystals at an Sb doping concentration of 0.1 mol % and Raman spectra of Sb-doped PbWO_4 crystals at different doping concentrations. This material is available free of charge via the Internet at <http://pubs.acs.org>.

References and Notes

- (1) (a) Lieber, C. M. *Solid State Commun.* **1998**, *107*, 607. (b) Peng, X. G.; Manna, L.; Yang, W. D.; Wickham, J.; Scher, E.; Kadavanich, A.; Alivisatos, A. P. *Nature* **2000**, *404*, 59. (c) El-Sayed, M. A. *Acc. Chem.*

- Res.* **2001**, 34, 257. (d) Templeton, A. C.; Wuelfing, W. P.; Murray, R. W. *Acc. Chem. Res.* **2000**, 33, 27. (e) Zhou, K. B.; Wang, X.; Sun, X. M.; Peng, Q.; Li, Y. D. *J. Catal.* **2005**, 229, 206.
- (2) Mdeleleni, M. M.; Hyeon, T. K.; Suslick, S. *J. Am. Chem. Soc.* **1998**, 120, 6189.
- (3) Gedanken, A. *Ultrason. Sonochem.* **2004**, 11, 47.
- (4) Okitsu, K.; Yue, A.; Tanabe, S.; Matsumoto, H.; Yobiko, Y.; Yoo, Y. B. *Chem. Soc. Jpn.* **2002**, 75, 2289.
- (5) Suslick, K. S.; Choe, S. B.; Cichowlas, A. A.; Grinstaff, M. W. *Nature* **1991**, 353, 414.
- (6) Kobayashi, M.; Ishii, M.; Usuki, Y. *Nucl. Instrum. Methods Phys. Res., Sect. A* **1998**, 406, 442.
- (7) Hara, K.; Ishii, M.; Kobayashi, M.; Nikl, M.; Takano, H.; Tanaka, M.; Tanji, K.; Usuki, Y. *Nucl. Instrum. Methods Phys. Res., Sect. A* **1998**, 414, 325.
- (8) Zhu, W. L.; Feng, X. Q.; Wu, Z. H.; Man, Z. Y. *Physica B* **2002**, 324, 53.
- (9) Nikl, M. *Phys. Status Solidi A* **2000**, 178, 595.
- (10) Liu, X. C. *Chin. Phys. Lett.* **1999**, 16, 761.
- (11) Li, W. S.; Tang, T. B.; Feng, X. Q. *J. Appl. Phys.* **2002**, 91, 136.
- (12) Kobayashi, M.; Usuki, Y.; Ishii, M.; Nikl, M. *Nucl. Instrum. Methods Phys. Res., Sect. A* **2002**, 486, 170.
- (13) Burachas, S.; Apanasenko, A.; Grinyov, B.; Ryzhikov, V.; Katrunov, K.; Starzhinskiy, M.; Ippolitov, M.; Manko, V.; Tamulaitis, G. *Int. J. Inorg. Mater.* **2001**, 3, 1101.
- (14) Chen, Y. H.; Shi, C. S.; Hu, G. Q. *J. Appl. Phys.* **2000**, 87, 1503.
- (15) Qu, X. D.; Zhang, L. Y.; Zhu, R. Y.; Deng, Q.; Liao, J. Y.; Yin, Z. W. *Nucl. Instrum. Methods Phys. Res., Sect. A* **2002**, 486, 89.
- (16) Xie, J. J.; Yang, P. Z.; Yuan, H.; Liao, J. Y.; Shen, B. F.; Yin, Z. W.; Cao, D. H.; Gu, M. *J. Cryst. Growth* **2005**, 275, 474.
- (17) Takai, S.; Touda, S.; Oikawa, K.; Mori, K.; Torii, S.; Kamiyama, T.; Esaka, T. *Solid State Ionics* **2002**, 148, 123.
- (18) Matijevic, E. *Chem. Mater.* **1993**, 5, 412.
- (19) Lin, Y.; Alexandridis, P. *J. Phys. Chem. B* **2002**, 106, 10834.
- (20) Barnes, T. J.; Prestidge, C. A. *Langmuir* **2000**, 16, 4116.
- (21) Yang, L.; Alexandridis, P. *Curr. Opin. Colloid Interface Sci.* **2000**, 5, 132.
- (22) Kabanov, A. V.; Batrakova, E. V.; Alakhov, V. Y. *J. Controlled Release* **2002**, 82, 182.
- (23) Ahmed, F.; Alexandridis, P.; Shankaran, H.; Neelamegham, S. *Thromb. Haemostasis* **2001**, 86, 1532.
- (24) Cohn, D.; Sosnik, A.; Levy, A. *Biomaterials* **2003**, 24, 3707.
- (25) Zhao, D.; Feng, J.; Huo, Q.; Melosh, N.; Fredrickson, G. H.; Chmelka, B. F.; Stucky, G. D. *Science* **1998**, 279, 548.
- (26) Han, Y. J.; Kim, J. M.; Stucky, G. D. *Chem. Mater.* **2000**, 12, 2068.
- (27) Karanikolos, G. N.; Alexandridis, P.; Itskos, G.; Petrou, A.; Mountziaris, T. J. *Langmuir* **2004**, 20, 550.
- (28) Kim, J. U.; Cha, S. H.; Shin, K.; Jho, J. Y.; Lee, J. C. *Adv. Mater.* **2004**, 16, 459.
- (29) Alexandridis, P.; Olsson, U.; Lindman, B. *Langmuir* **1998**, 14, 2627.
- (30) Ivanova, R.; Lindman, B.; Alexandridis, P. *Langmuir* **2000**, 16, 9058.
- (31) For a comprehensive review, see: Alexandridis, P.; Hatton, T. A. *Colloids Surf., A* **1995**, 96, 1.
- (32) (a) Warshawsky, A.; Kalir, R.; Deshe, A.; Berkovitz, H.; Patchornik, A. *J. Am. Chem. Soc.* **1979**, 101, 4249. (b) Sakai, T.; Alexandridis, P. *J. Phys. Chem. B* **2005**, 109, 7766.
- (33) (a) Puentes, V. F.; Zanchet, D.; Erdonmez, C. K.; Alivisatos, A. P. *J. Am. Chem. Soc.* **2002**, 124, 12874. (b) Puentes, V. F.; Krishnan, K. M.; Alivisatos, A. P. *Science* **2001**, 291, 2115.
- (34) Qi, L.; Cölfen, H.; Antonietti, M. *Angew. Chem., Int. Ed.* **2000**, 39, 604.
- (35) Marentette, J. M.; Norwig, J.; Stockelmann, E.; Meyer, W. H.; Wegner, G. *Adv. Mater.* **1997**, 9, 647.
- (36) Lin, Y.; Alexandridis, P. *J. Phys. Chem. B* **2002**, 106, 10834.
- (37) Hayes, D.; Meisel, D.; Micic, O. I. *Colloids Surf.* **1991**, 55, 121.
- (38) Liu, B.; Yu, S. H.; Li, L. J.; Zhang, Q.; Zhang, F.; Jiang, K. *Angew. Chem., Int. Ed.* **2004**, 43, 4745.
- (39) (a) Penn, R. L.; Banfield, J. F. *Science* **1998**, 281, 969. (b) Banfield, J. F.; Welch, S. A.; Zhang, H. Z.; Ebert, T. T.; Penn, R. L. *Science* **2000**, 289, 751.
- (40) Penn, R. L.; Oskam, G.; Strathmann, T. J.; Searson, P. C.; Stone, A. T.; Veblen, D. R. *J. Phys. Chem. B* **2001**, 105, 2177.
- (41) (a) Liu, B.; Zeng, H. C. *Small* **2005**, 1, 566. (b) Kahlweit, M. *Angew. Chem., Int. Ed. Engl.* **1965**, 4, 444. (c) Ostwald, W. Z. *Phys. Chem.* **1900**, 34, 495.
- (42) Doktycz, S. J.; Suslick, K. S. *Science* **1990**, 247, 1067.
- (43) Crane, M.; Frost, R. L.; Williams, P. A.; Klopogge, J. T. *J. Raman Spectrosc.* **2002**, 33, 62.
- (44) Ross, S. D. *Inorganic Infrared and Raman Spectra*; McGraw-Hill: Maidenhead, U.K., 1972.
- (45) Bastians, S.; Crump, G.; Griffith, W. P.; Withnall, R. *J. Raman Spectrosc.* **2004**, 35, 726.
- (46) Belsky, A. N.; Mikhailin, V. V.; Vasil'ev, A. N.; Dafinei, I.; Lecoq, P.; Pedrini, C.; Chevallier, P.; Dhez, P.; Martin, P. *Chem. Phys. Lett.* **1995**, 243, 552.
- (47) Yu, M.; Lin, J.; Fang, J. *Chem. Mater.* **2005**, 17, 1783.
- (48) Bae, J. S.; Kim, S. B.; Jeong, J. H.; Park, J. C.; Kim, D. K.; Byeon, S. H.; Yi, S. S. *Thin Solid Films* **2005**, 471, 224.
- (49) Soledade, L. E. B.; Longo, E.; Leite, E. R.; Pontes, F. M.; Lanciotti, F.; Campos, C. E. M.; Pizani, P. S.; Varela, J. A. *Appl. Phys. A* **2002**, 75, 629.